Environmental Science & Technology

pubs.acs.org/est

Article

Relative Insignificance of Polyamide Layer Selectivity for Seawater Electrolysis Applications

Xuechen Zhou, Le Shi, Rachel F. Taylor, Chenghan Xie, Bin Bian, Cristian Picioreanu, and Bruce E. Logan*

Cite This: *Environ. Sci. Technol.* 2023, 57, 14569−14578

Read Online

ACCESS | Metrics & More | Article Recommendations | Supporting Information

ABSTRACT: Low-cost polyamide thin-film composite (TFC) membranes are being explored as alternatives to cation exchange membranes for seawater electrolysis. An optimal membrane should have a low electrical resistance to minimize applied potentials needed for water electrolysis and be able to block chloride ions present in a seawater catholyte from reaching the anode. The largest energy loss associated with a TFC membrane was the Nernstian overpotential of 0.74 V (equivalent to 37 Ω cm^2 at 20 mA cm^{-2}), derived from the pH difference between the anolyte and catholyte and not the membrane ohmic overpotential. Based on analysis using electrochemical impedance spectroscopy, the pristine TFC membrane contributed only 5.00 Ω cm^2 to the ohmic resistance. Removing the polyester support layer reduced the resistance by 79% to only 1.04 Ω cm^2, without altering the salt ion transport between the electrolytes. Enlarging the pore size (∼5 times) in the polyamide active layer minimally impacted counterion transport across the membrane during electrolysis, but it increased the total concentration of chloride transported by 60%. Overall, this study suggests that TFC membranes with thinner but mechanically strong supporting layers and size-selective active layers should reduce energy consumption and the potential for chlorine generation for seawater electrolyzers.

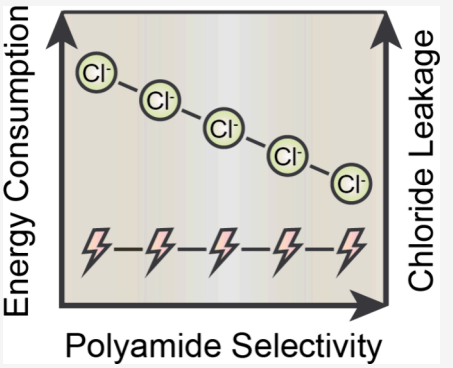

KEYWORDS: *green hydrogen, seawater electrolysis, energy consumption, chloride leakage, thin-film composite membrane, polyamide selectivity*

INTRODUCTION

Hydrogen (H_2) gas generation through water electrolysis using renewable electricity can reduce its carbon footprint compared to conventional steam reforming, but currently water electrolysis is two to four times more expensive.[1,2] In addition, optimal locations for renewable electricity generation supplied by solar and wind energy[3,4] do not always coincide with the availability of freshwater sources.[5] For instance, coastal areas can provide excellent conditions for wind energy sources, but such locations may have limited freshwater availability. While seawater can be desalinated for use in water electrolyzers, this additional process can add to the cost of the H_2 production as well as increase operational complexity.[6,7] An alternative strategy is to directly use seawater for water electrolysis.[8,9] However, exposing the anode to chloride ions present in seawater will result in the generation of toxic chlorine gas, which can also damage the electrolyzer components.

An asymmetric electrolyzer configuration to enable the use of seawater as the catholyte was recently proposed based on using low-cost (<$10 m^{-2}) polyamide (PA) thin-film composite (TFC) membranes. Typical TFC membranes can reject >99% of the salt in the feed stream during the reverse osmosis process.[10,11] Therefore, when seawater is only used for the catholyte and nonreactive salts such as sodium perchlorate are used for the anolyte, TFC membranes can effectively limit the transport of chloride or other salt ions in seawater from the catholyte into the anolyte and perchlorate ion transport from the anolyte to the catholyte (Figure 1).[9] This asymmetric electrolyte configuration thus minimizes the generation of chlorine gas. Despite their retention of salt ions, TFC membranes are permeable to water ions (H^+ and OH^-), so charge can be balanced using water ions during water electrolysis.[12] Using cation exchange membranes, which are commonly used as separators in water electrolyzers due to their high ionic conductivity,[13−15] in the same asymmetric configuration can also reduce the chloride permeation,[16] but these membranes can be expensive (∼$250 to 500 m^{-2} or more) and facilitate cation transport in either direction across the membrane.[7]

The factors that impact ion crossover during electrolysis, especially the transport of water ions, are not well studied

Received: June 21, 2023
Revised: September 2, 2023
Accepted: September 5, 2023
Published: September 18, 2023

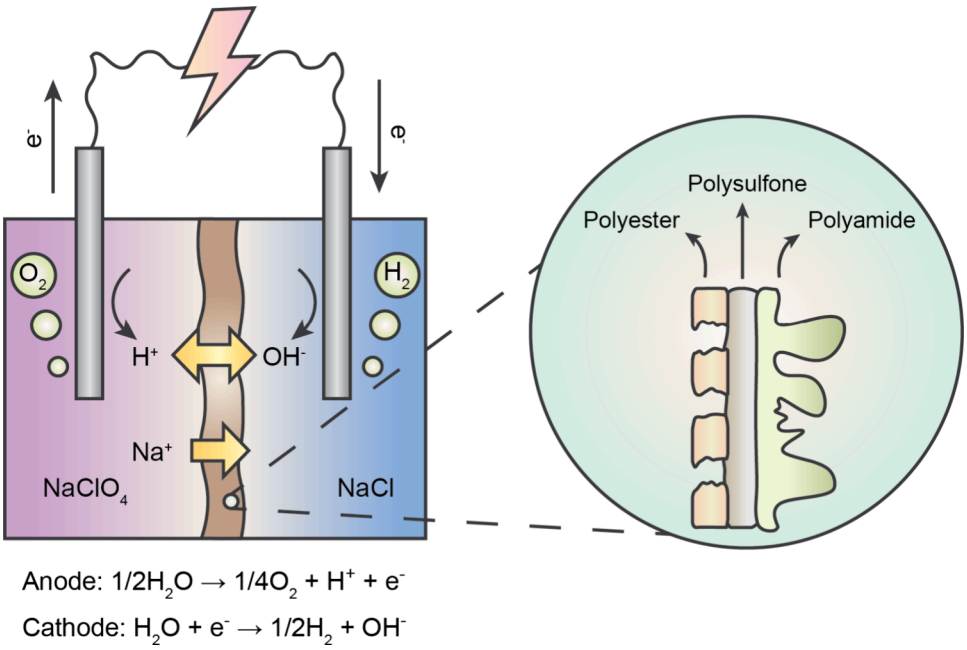

Figure 1. Schematic diagram showing the use of the PA TFC membranes for seawater electrolysis. Sodium perchlorate is used in the anolyte, and artificial seawater (sodium chloride) is used in the catholyte. Water oxidation occurs on the anode, releasing oxygen gas and H^+. Water reduction occurs on the cathode, producing H_2 gas and OH^- ions. Charge is balanced by the transport of hydrated salt ions (mainly Na^+ and Cl^-) and water ions (H^+ and OH^-) through the composite membrane. A typical TFC membrane is composed of three polymeric layers: the PA active layer, the polysulfone support layer, and the polyester nonwoven fabric structural support layer.

because TFC membranes are usually used for desalination at near-neutral pH and under conditions where there is a large water flux through the membrane. In contrast, when TFC membranes are used in water electrolyzers, there is a large pH gradient across the membrane due to the production of H^+ in the anolyte and OH^- in the catholyte, with minimal water transport between the chambers. A typical PA TFC membrane is composed of three polymeric layers: a PA active layer, a polysulfone (PSF) support layer, and a polyester (PET) nonwoven fabric structural support layer (Figure 1).[10] Ion transport could be impacted differently by each layer of the TFC membrane in an electric-field-driven water electrolyzer compared with a pressure-driven desalination system. In a pressure-driven filtration process, the PA active layer plays a dominant role in separating water and salt ions, the PSF layer provides support for the PA layer, and the PET layer gives mechanical strength to the membrane.[17] The PET layer is not needed in the absence of high pressures, for example, in forward osmosis applications.[18] In a seawater electrolyzer, the electric field and concentration gradients will drive ion transport through the membrane, during which charge will be balanced by water ions (H^+ at low pH and OH^- at high pH) and leakage of hydrated salt ions (Na^+ and Cl^-). However, it is not known how the relative transport of these ions is impacted by different TFC layers (Figure 1). This selective transport between hydrated ions and water ions will further affect the energy consumption during the electrolysis not only through the membrane charge transfer resistance (i.e., ohmic overpotential), but also by building up the pH gradient between the electrolytes (i.e., Nernstian overpotential). A better understanding of the dependence of ion transport on membrane properties is thus needed to help reduce the energy losses in seawater electrolysis.

The impact of the PET structural and PA active layers was examined here on the energy consumption and chloride transport during seawater electrolysis. The effect of the thickness of the PET layer was determined by either removing that layer or adding one or two additional layers to the membrane. The role of the active layer was further examined by increasing the pore size using a treatment with chlorine. The extent of salt ion permeation was quantified by measuring the concentrations of the salt ions in the opposing chambers over time. Based on these results, we were able to obtain a better understanding of the mechanisms impacting ion transport through TFC membranes driven by an electric field during water electrolysis.

MATERIALS AND METHODS

Materials and Chemicals. All tests were conducted using SW30 TFC membranes (Dow Chemical) with an indicated 99.5% salt rejection (manufacturer's specification). The chemicals and sources were reagent-grade sodium hypochlorite (available chlorine 4.00−4.99%, Sigma-Aldrich); sodium perchlorate (anhydrous, 98.0−102.0%) and potassium chloride (99.0%, Thermo Fisher Scientific); and hydrochloric acid (ACS grade) and perchloric acid (ACS grade, VWR). Deionized (DI) water (>18.2 MΩ cm) used for preparation of all solutions was produced using a Milli-Q ultrapure water purification system (Synergy).

Membrane Preparation. SW30 membranes were immersed in 25% (v/v) isopropyl alcohol solution for 30 min to remove any extractable preservatives and components and to fully wet the membranes. These membranes were then thoroughly washed with DI and stored at 4 °C for further use. The support layer of the SW30 membranes was removed for tests by gently peeling off the PET fabric backings using tweezers. Additional PET layers were added by physically compressing them to the back of the pristine SW30 membranes. The active layer of the membranes was treated

https://doi.org/10.1021/acs.est.3c04768
Environ. Sci. Technol. 2023, 57, 14569−14578

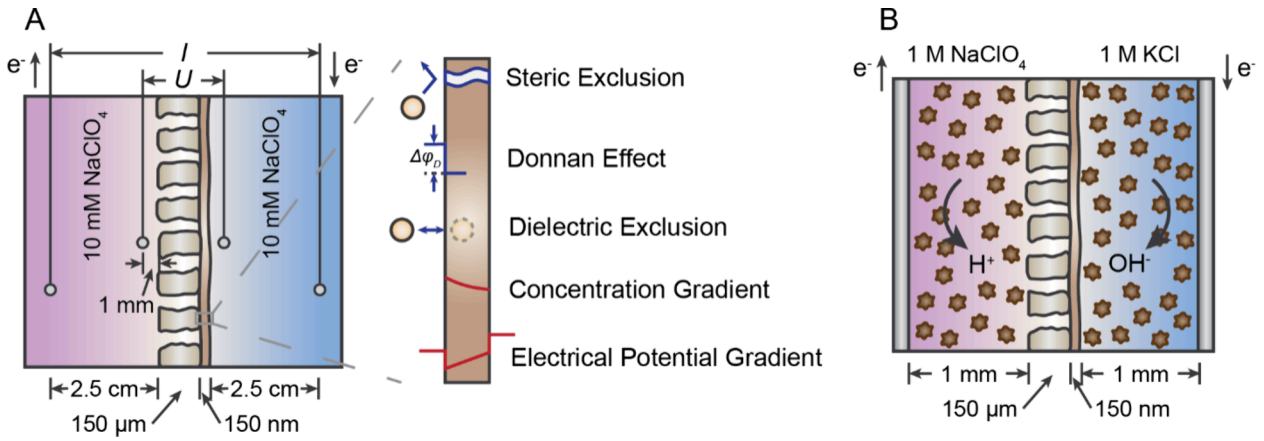

Figure 2. (A) Schematic diagram showing the modeling of membrane resistance with 10 mM $NaClO_4$ as the electrolyte. (B) Schematic diagram showing the modeling of ion transport within the electrolytic cell using 1 M $NaClO_4$ in the anolyte and 1 M KCl in the catholyte. Stars represent platinum-decorated carbon electrodes.

to reduce the cross-linking ratio by immersing the membranes in 2000 ppm of NaClO solutions (pH = 10) for 0.5, 2, or 24 h.[19,20] The reduced cross-linking ratio resulted in increased pore sizes and porosities of the active layer.

Membrane Resistance Measurements. The ionic resistance of each membrane was characterized by using a standard four-electrode method. Briefly, a membrane coupon (area of 7.0 cm^2) was assembled into a two-chamber cubic-shaped reactor containing a cylindrical cross-sectional area (Figure S1). Each chamber was filled with 30 mL of an electrolyte (10 mM $HClO_4$ or $NaClO_4$). Platinum-coated titanium mesh electrodes (4.4 cm^2 projected area) were placed on both ends of the reactor. Two Ag/AgCl reference electrodes (3 M KCl, BASi West Lafayette, IN) were inserted into the Luggin Capillaries on both sides of the membranes. The end tips of the capillaries were 1 mm away from the membrane surface. Constant currents (−0.086, −0.064, −0.043, 0.00, 0.021, 0.043, and 0.064 mA cm^{-2}) were applied between two platinum-coated titanium mesh electrodes at 30 s intervals by using a potentiostat (Biologic VMP3), with the potential difference across the membrane monitored by using the reference electrodes. Slopes of the obtained $I-V$ curves provided resistance of the electrolyte and membrane ($R_{sol+mem}$). This experiment was then repeated with the same electrolytes but without the membranes (R_{sol}) so that the membrane resistance could be calculated by difference.

Seawater Electrolyzer Operation. The applied voltage needed to obtain a set current in the electrolyzer was examined for different membranes using a zero-gap flow cell (Scribner, North Carolina; Figure S2). Carbon cloth (2 × 2 cm^2) coated with 10% Pt/C catalyst was used for both electrodes for simplicity of electrode preparation (as opposed to more optimal or nonprecious metal options; see Text S1 for electrode preparation), with the catalyst layer facing the membrane. Membranes were assembled between the two electrodes, with the PA active layer facing the cathode. This sandwich structure was pressed together using end plates and tightened with a torque wrench to 9 N m. Different cations and anions were used for the electrolytes to measure salt ion crossover, with 1 M $NaClO_4$ used for the anolyte and 1 M KCl for the catholyte. Both electrolytes (100 mL each) were circulated at a flow rate of 15 mL min^{-1} by using a peristaltic pump. Chronopotentiometry (CP) tests were conducted using the potentiostat at a current density of 20 mA cm^{-2} for 8 h. Samples (1 mL) were collected from both the anolyte and catholyte at different time intervals for ion crossover tests. The concentrations of Na^+ and ClO_4^- ions in the catholyte and K^+ and Cl^- ions in the anolyte were analyzed using ion chromatography (Dionex, Thermo Fisher Waltham, MA). The pH of both electrolytes was measured at the conclusion of the experiment.

Energy Loss Analysis. During electrolyzer operation, H^+ is generated at the anode, and OH^- is generated at the cathode. When some of the cross-membrane charge is carried by salt ions, only a portion of the produced water ions will be used to carry the charge across the membrane. The remaining water ions will accumulate within the respective electrolytes to maintain the bulk charge neutrality, producing a large pH difference across the membrane. The difference in pH between the anolyte and catholyte, referred to here as the Nernstian loss, contributed to an additional operating voltage needed for electrolysis.[6] To calculate the Nernstian loss of each water electrolyzer, the pH of the catholyte (pH_{Cat}) and anolyte (pH_{An}) was measured after the operation. The Nernstian Loss (E_{Nernst}) was calculated by[21]

$$E_{Nernst} = 0.059(pH_{Cat} - pH_{An}) \quad (1)$$

The membrane and solution contribute an additional ohmic resistance (R_Ω) to the total applied potential needed for water electrolysis.[6] This total ohmic loss (E_Ω) was measured using electrochemical impedance spectroscopy (EIS) with the value of the scan intercept in the Nyquist plots as

$$E_\Omega = iR_\Omega \quad (2)$$

where i is the applied current density.

Modeling the Ionic Resistance of PA TFC Membranes. A one-dimensional (1-D) time-dependent numerical model was set up to represent the four-probe system, and it was implemented in COMSOL Multiphysics (version 5.5). The model was used to calculate the dependence of the membrane resistance on the PA layer pore size, with 10 mM $NaClO_4$ used as both the anolyte and catholyte (Figure 2A), exposed to a constant current.

Geometry. 1-D concentration and potential gradients were computed in four connected domains. Two electrolyte compartments, each with a 2.5 cm gap between the electrode and membrane surface, were separated by a weakly charged

https://doi.org/10.1021/acs.est.3c04768
Environ. Sci. Technol. 2023, 57, 14569−14578

membrane with the active layer of 150 nm facing the catholyte and a homogeneous backbone of 150 μm facing the anolyte (Figure 2A). The Pt/Ti mesh electrodes used experimentally were only included as boundaries to the electrolyte domains because being located far from the membrane we assumed that electrode dynamics would not impact ion transport through the membrane. Two system "point probes" were used to measure the computed potential 1 mm away from either side of the membrane during the 30 s of current passage, just as the reference electrodes with Luggin capillaries do experimentally. In the way the solution resistance and combined solution and membrane resistance were measured experimentally, we simulated both scenarios and calculated the membrane resistance with Ohm's law using the measured potential drop between the point probes. Values of the model parameters are listed in Table S1.

Ion Transport with Charge Balance. Four ions i were considered: Na^+ and ClO_4^- from the salt and water ions H^+ and OH^- with molar concentrations c_i. Ion transport through all domains was assumed to occur by diffusion and electromigration, represented by time-dependent mole balances based on Nernst−Planck fluxes:

$$\frac{\partial c_i}{\partial t} = f_i D_i \frac{\partial}{\partial x}\left(\frac{\partial c_i}{\partial x} + z_i c_i \frac{F}{RT}\frac{\partial \phi}{\partial x}\right) \quad (3)$$

Ion diffusion coefficients D_i in anolyte and catholyte took values similar to those in water ($f_i = 1$). In the membrane backbone, these were reduced to 10% of their value in water to account for porosity ($f_i = 0.1$). Through the active layer, the ion transport was affected by friction with the charged membrane (solution friction model[17]) so that $f_i = K_{d,i}\varepsilon$ with hindrance factor $K_{d,i}$ and effective active layer porosity ε. The charge balance must also hold at any point x, expressed as electroneutrality conditions including ion charges z_i in all domains and additionally the negative membrane charge in the active layer domain:

$$\sum_i z_i c_i = 0(\text{electrolytes}),\ \sum_i z_i c_i - c_m = 0(\text{active layer}) \quad (4)$$

The membrane change density c_m was a computed function of the local pH in the active layer as $c_m = c_{m,c}K_{a,c}/(c_{H+} + K_{a,c}) - c_{m,a}c_{H+}/(c_{H+} + K_{a,a})$, where $c_{m,c}$ is the total density of carboxyl groups having an ionization constant $K_{a,c}$, $c_{m,a}$ is the total density of protonated amine groups with $K_{a,a}$, and c_{H+} is the local molar proton concentration.[22] The water dissociation equilibrium $K_w = c_{H+}c_{OH-}$ is also imposed at each position x, which allows for computing the local pH.

Boundary Conditions and Ion Partitioning. Boundary conditions were set at the electrode surfaces: a fixed current density at the anode $i_a = 0.07$ mA cm^{-2} and a reference electrolyte potential at the cathode $\phi = 0$ V, together with zero-flux conditions for all ion components. In these conditions, the current density remains constant over the whole electrolyte, $i(x) = i_a$. At the two sides of the active layer, ion partition was considered by three mechanisms: steric exclusion, Donnan effect, and dielectric exclusion, so that the concentration on the membrane side $c_{i,m}$ is related to concentration in the water phase $c_{i,w}$ by $c_{i,m} = c_{i,w}\Phi_{st,i}\Phi_{D,i}\Phi_{B,i}$. Assuming spherical ions and cylindrical pores, the steric partition factor can be estimated from[23] $\Phi_{st,i} = (1 - \lambda_i)^2$, with λ_i being the ratio between ion Stokes radius r_i and pore radius r_p. The Donnan electrostatic partition is determined by the potential difference on the two sides of the interface, $\Phi_{D,i} = \exp\left(-\frac{z_i F}{RT}\Delta\phi\right)$. The dielectric partitioning can be expressed as[24] $\Phi_{B,i} = \exp\left(-\frac{\Delta W_i}{k_B T}\right)$, where k_B is the Boltzmann constant, T is the absolute temperature, and $\Delta W_i = \frac{z_i^2 e^2}{8\pi\varepsilon_0 r_p}\left(\frac{1}{\varepsilon_m} - \frac{1}{\varepsilon_w}\right)$ is the Born energy barrier,[25] when ions move from water to a membrane medium with a low dielectric constant (with e being the elemental charge, ε_0 being the vacuum permittivity, ε_m being the dielectric constant in the membrane pore, and ε_w being the dielectric constant for the bulk solution). Among these three mechanisms, steric exclusion and dielectric exclusion are directly impacted by the active layer (PA) pore size.

Initial Conditions. The initial values of concentration conditions were set according to the experimental conditions: $c_{0,Na+} = c_{0,ClO4-} = 0.01$ M at pH 5.7 and thus $c_{0,H+} = 10^{-pH}$ and $c_{0,OH-} = K_w/c_{0,OH-}$.

Solution. The system of balance equations with the associated initial and boundary conditions was solved for a period of 30 s on a fine mesh (50 μm in electrolytes and 20 nm in the active layer).

Modeling the Ion Permeation within the Electrolytic Cell. Permeation of six ions (Na^+, K^+, Cl^-, ClO_4^-, H^+, and OH^-) through TFC membranes during the electrolysis was described using generally the same approach as in the case of modeling the membrane resistance. Parameters used in the model are provided in Table S1.

Geometry and Ion Transport. Diffusion−electromigration eqs 3 and 4 (with the other constitutive equations) were applied through the membrane active and support layers (Figure 2B). In this case, however, carbon electrodes with a thickness of 1 mm each were assembled next to the membrane, both described as stagnant layers filled with electrolyte and reduced porosity so that $f_i = \varepsilon_{elec}$. Generation of H^+ at the anode and OH^- at the cathode was considered by a volumetric electrochemical reaction resulting from applying a constant current density $i_a = 20$ mA cm^{-2} in electrodes having a specific surface area a_v so that $r_{e,H+} = r_{e,OH-} = i_a a_v/F$ in the respective anode and cathode domains.

Boundary Conditions. The electrolyte reference potential at the cathode was set to $\phi = 0$ V, while zero-flux and insulation conditions were applied for all ions at the lateral anode/cathode boundaries. The partition conditions were the same as those for computing resistance. Concentrations of salt ions in the electrodes furthest away from the membrane (K^+ and Cl^- at $x = 0$ boundary; Na^+ and ClO_4^- at $x = 2.15$ mm boundary) were collected over time to calculate the ion transport within the electrolytic cell.

Initial Conditions. The initial values of concentration conditions were also set according to the experimental conditions, pH 5.7, in all electrolyte and membrane domains ($c_{0,H+} = 10^{-pH}$, $c_{0,OH-} = K_w/c_{0,OH-}$). The anode electrode domain initially contained only 1 M $NaClO_4$ ($c_{0,Na+} = c_{0,ClO4-} = 1$ M and $c_{0,K+} = c_{0,Cl-} = 0$), while the cathode contained only 1 M KCl ($c_{0,K+} = c_{0,Cl-} = 1$ M and $c_{0,Na+} = c_{0,ClO4-} = 0$). The initial electrolyte potential was nearly zero. The model

https://doi.org/10.1021/acs.est.3c04768
Environ. Sci. Technol. 2023, 57, 14569−14578

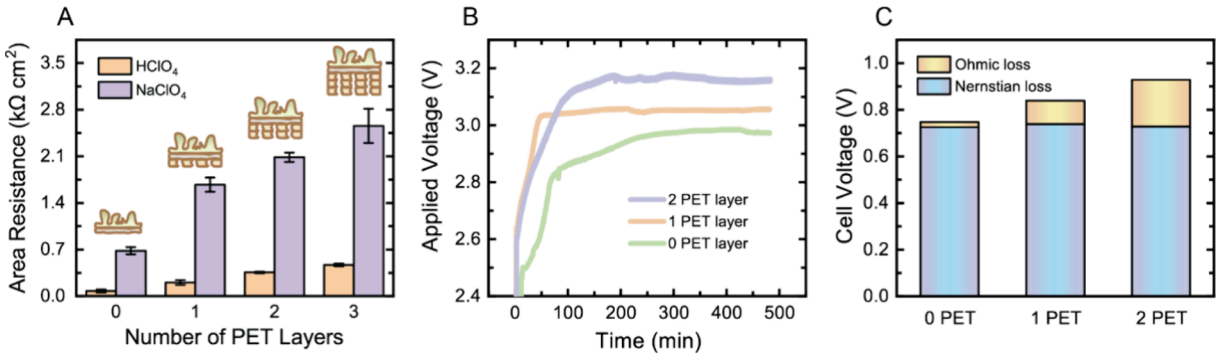

Figure 3. Seawater electrolyzer performance with TFC membranes with a variable number of PET layers. (A) Measured membrane area resistance using either $NaClO_4$ or $HClO_4$ (10 mM) electrolytes. (B) Applied voltages needed for electrolyzer operation at a current density of 20 mA cm^{-2} using solutions of 1 M $NaClO_4$ as the anolyte and 1 M KCl as the catholyte. (C) Voltage losses in electrolyzer tests for the Nernstian and ohmic resistances.

equations were solved for a period of 1 h from these initial conditions.

RESULTS AND DISCUSSION

Impact of Support Layer Thickness on Seawater Electrolyzer Overpotential. The ionic resistance of membranes measured with either $HClO_4$ or $NaClO_4$ electrolytes in electrochemical test cells increased with the number of PET layers (Figure 3A). With the PET layer removed, the membrane resistance with $HClO_4$ was 77 ± 24 Ω cm^2. This resistance then increased to 205 ± 36 Ω cm^2 (1 layer), 357 ± 13 Ω cm^2 (2 layers), and 470 ± 21 Ω cm^2 (3 layers). The magnitudes of these increases are consistent with the resistance of the PET layer measured in a separate experiment with $HClO_4$ (125 ± 21 Ω cm^2). Considering the significantly higher mobility of H^+ (36.2×10^{-8} m^2 s^{-1} V^{-1})[26] compared to much larger ClO_4^- ions (5.7×10^{-8} m^2 s^{-1} V^{-1}),[27] the membrane resistance measured with the acidic medium ($HClO_4$) mainly reflects the properties of H^+ transport. In the tests with salt ($NaClO_4$), the membrane resistance was much higher, ranging from 682 ± 54 Ω cm^2 (no PET) to 2560 ± 260 Ω cm^2 (3 PET). These results show that when there is a high concentration of Na^+ ions using $NaClO_4$, and a low H^+ concentration due to the near-neutral pH, the resistance increased due to charge being balanced by the transport of hydrated salt ions (Na^+ and ClO_4^-) compared to H^+ using the acidic $HClO_4$ electrolyte.

The applied voltage needed to maintain a set current density of 20 mA cm^{-2} in electrolyzer tests (1 M $NaClO_4$ anolyte and 1 M KCl catholyte) increased with the number of PET layers (Figure 3B), consistent with the trends observed in the electrochemical cell tests. With a TFC membrane containing the original PET layer, the applied voltage at steady state (400−480 min) was 3.053 ± 0.002 V. This value was decreased to 2.978 ± 0.005 V by removing the PET layer, and it increased to 3.155 ± 0.002 V with 2 PET layers. Different from the application of TFC membranes for filtration where the PET layer mainly provides mechanical support, these results show the important contribution of the PET layer to increasing the electrical resistances and thus the higher applied voltages needed.

The components of the energy loss associated with membranes in the water electrolyzer in the presence and absence of PET layers were further examined in terms of the Nernstian and ohmic losses in each test. When using the pristine PA membrane, the final pH of the anolyte was 0.7 and the final pH of the catholyte was 13.2, leading to a calculated Nernstian overpotential of 0.74 V (equivalent to 37 Ω cm^2 at 20 mA cm^{-2}) during the electrolysis (Figures S3A and 3C).[6] No appreciable change in the final electrolyte pH was measured when the number of PET layers was varied (Figure S3A), resulting in a similar Nernstian overpotential (0.73 V for both the electrolyzers with the 0-PET-layer membrane and the 2-PET-layer membrane, Figure 3C). The independence of the Nernstian loss on the PET layer thickness is attributable to the fact that the PET layers do not produce selective transport between Na^+ and H^+ ions, as expected from a barrier with a pore size much larger than the ion size. The ohmic resistance in the electrolyzer increased from 1.04 to 10.0 Ω cm^2 (Figure S4A), resulting in an increase in the potential needed for the membrane charge transfer from 0.021 to 0.20 V at an applied current of 20 mA cm^{-2} (Figure 3C), consistent with the observed increase in the total applied voltage. The dominant contribution to the overpotential related to the membranes was therefore the Nernstian loss due to the pH difference (Figure 3C).

Impact of the Active Layer Selectivity on Electrolyzer Overpotential. Considering that the Nernstian loss was caused by the leakage of salt ions and the accumulation of H^+ within the anolyte, the impact of the active layer selectivity toward the transport of salt and water ions on the electrolyzer performance was then studied by increasing the PA layer pore size. When the amide bonds within the PA layer were cleaved by chlorine treatment (Figure 4A), the membrane resistance decreased slightly when measured in $HClO_4$ (Figure 4B). For example, at the longest treatment time, the resistance decreased by 14% to 177 ± 5 Ω cm^2, compared to 205 ± 36 Ω cm^2 for the pristine membrane. The decrease in resistance due to chlorine treatment was much more apparent when using the $NaClO_4$ electrolyte, with a decrease of 67% to 555 ± 35 Ω cm^2 compared to the control (no treatment) of 1670 ± 110 Ω cm^2. The greater impact on the resistance to Na^+ passage compared to that of the smaller H^+ showed the importance of the pore size (Figure 4C). Large hydrated salt ions (such as Na^+ ions) experienced higher resistance during their permeation through subnanometer pores.[11,28] Therefore, when the steric confinement was relaxed by increasing the pore size, the ion permeation rate increased, and so did the membrane conductance. For H^+ transport, ion hopping is a unique mechanism that facilitates the H^+ transport within

https://doi.org/10.1021/acs.est.3c04768
Environ. Sci. Technol. 2023, 57, 14569−14578

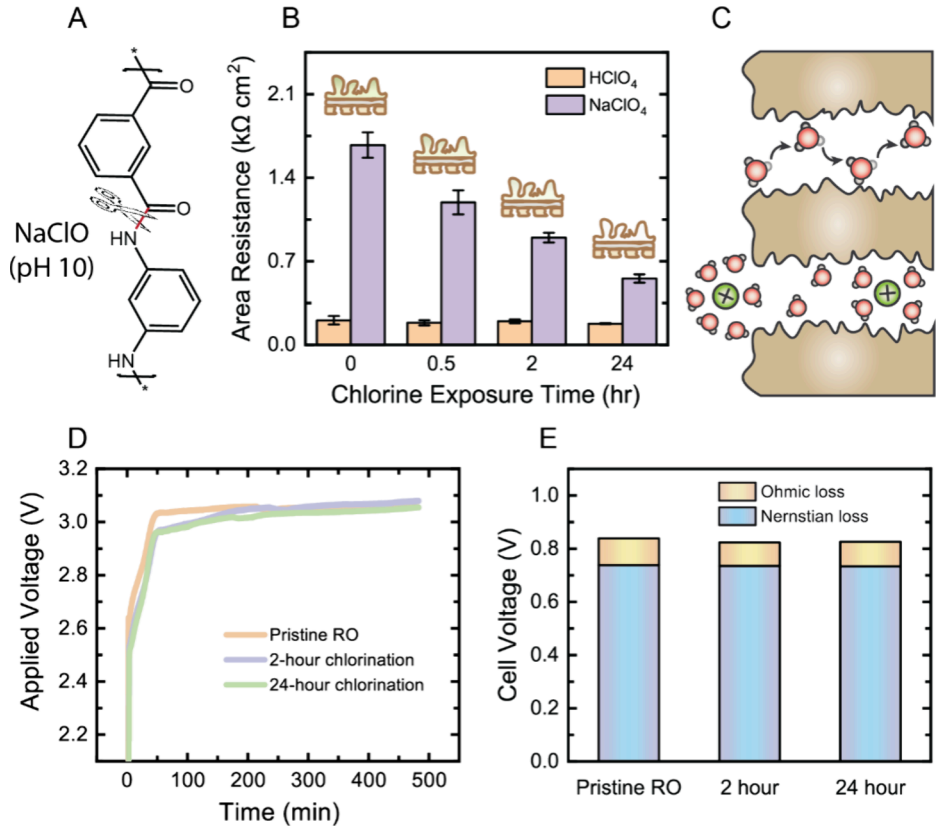

Figure 4. Seawater electrolyzer performance with PA TFC membranes treated with NaClO for varied durations. (A) Cleavage of the amide bonds occurred when treating the PA layer with NaClO. (B) Measured resistance of the PA TFC membranes treated with NaClO for different durations. (C) Schematic diagram showing the mechanisms proposed for the transport of H^+ and hydrated ions (e.g., Na^+) through the subnanometer pores; top: ion-hopping, bottom: permeation with dehydration. (D) Applied voltage for the seawater electrolyzer assembled with PA TFC membranes treated with NaClO for varied durations. (E) Voltage loss analysis for the seawater electrolyzer assembled with PA TFC membranes treated with NaClO for different durations.

aqueous solutions.[29,30] Thus, H^+ transport appears to be less sensitive to the pore size as long as continuous water strings are formed within the pores to enable H^+ hopping.

The applied voltage needed for water electrolysis at 20 mA cm^{-2} under steady conditions (400−480 min) was independent of the changes in the pore size within the PA layer (Figure 4D). With 2 h of treatment with NaClO, the applied voltage was 3.072 ± 0.004 V, compared to 3.047 ± 0.004 V after 24 h of treatment and 3.053 ± 0.002 V for the pristine PA membrane. In a pressure-driven filtration process, the PA layer of the TFC membrane determines its separation capability and energy consumption.[31] In contrast, in the water electrolyzer, enlarging the PA pore size did not result in a change in the applied voltage needed to achieve the set current density.

Further analysis of the energy losses associated with membranes in the electrolyzer indicated that the sum of the Nernstian and ohmic losses also remained nearly constant with the changes in PA pore sizes (Figure 4E). The ohmic resistance was measured to be 5.0 Ω cm^2 for the electrolyzer assembled with the pristine PA membrane, compared to 4.4 Ω cm^2 with the PA membrane treated with NaClO for 2 h and 4.6 Ω cm^2 when treated for 24 h (Figure S4B). At the current density of 20 mA cm^{-2}, the ohmic overpotential was calculated to be 0.10 V (no treatment), 0.088 V (2 h treatment), and 0.092 V (24 h treatment) (Figure 4E), while the estimated Nernstian loss was the same, 0.74 V, for all treated and untreated membranes (Figure 4E). Overall, these results show that the PA layer selectivity of the composite membranes had a limited impact on the energy required for operation of the seawater electrolyzer.

Impact of the Active Layer Pore Size on Ion Crossover. For all of the salt ions, there was a linear increase in ion concentrations over time in the opposing chamber, when using a TFC membrane as the separator (Figure 5A,B). The lack of change in the rate of ion transport also demonstrates the stable membrane integrity during the electrolysis. Among four salt ions within the system, there was significant Na^+ ion crossover from the anolyte to the catholyte and Cl^- transport to the anolyte in the direction of the electric field, but the permeation of K^+ and ClO_4^- ions was negligible in the opposite direction. During electrolysis, the cross-membrane transport of Na^+ and Cl^- ions is driven by both the concentration gradient and the electric field. However, for the permeation of K^+ and ClO_4^- ions, the concentration gradient is the driving force, as their charges are the opposite of the direction of the electric field. Thus, these ions are better retained in their respective compartments. The limited K^+ and ClO_4^- permeation compared to Na^+ and Cl^- ions demonstrates that the electro-driven process is the predominant mechanism governing the ion transport during electrolysis.

The crossover of Na^+ ions was notably higher than that of Cl^- ions despite the lower mobility of Na^+ ions (5.19×10^{-8} m^2 s^{-1} V^{-1}) compared to Cl^- ions (7.91×10^{-8} m^2 s^{-1} V^{-1}),

https://doi.org/10.1021/acs.est.3c04768
Environ. Sci. Technol. 2023, 57, 14569−14578

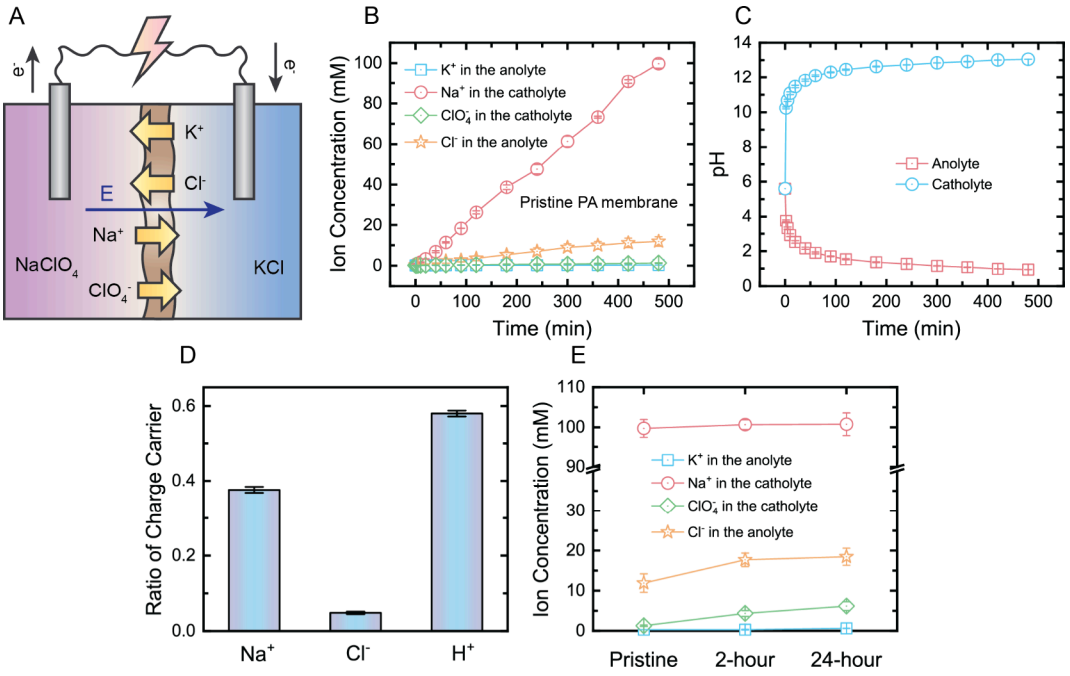

Figure 5. (A) Schematic diagram showing the direction of the electric field and ion permeation within the electrolyzer. (B) Ion permeation through the pristine PA membrane during the electrolysis. (C) pH changes of the catholyte and anolyte within the electrolyzer assembled with the pristine PA membrane. (D) Fraction of charge carried by Na^+, Cl^-, and H^+ within the electrolyzer assembled with the pristine membrane at the steady state. (E) Change of final ion concentrations (at 8 h) within a water electrolyzer due to the PA layer pore enlargement with chlorine.

which may be due to the expected net negative charge of the PA layer under these operational conditions. The pH of the catholyte, calculated based on the measured ion permeation and charge balance, increased rapidly during the first hour of operation, reaching 12.0 (Figure 5C), and then quickly stabilized at a pH of 13.1, close to the final pH measured with the pH probe (13.2). The PA TFC membrane was oriented with the PA active layer facing the catholyte. At pH 13.1, the PA layer will be negatively charged due to the deprotonation of its carboxyl groups.[32] Thus, Na^+ (membrane counterions) transport preferentially compared to Cl^- (co-ions) due to electrostatic interaction. At steady state, 58% of the charge transported through the PA membrane was carried by water ions (simplified as H^+ here), followed by Na^+ (37% of the charge transfer), and the remaining 5% charge was carried by Cl^- (Figure 5D). These results on ion transport suggest that the membrane charge transfer resistance is mainly dominated by resistance to H^+ transport.

When the pore size of the PA layer was enlarged with chlorine treatment, similar trends were recorded in the cation permeation during electrolysis (Figure S6). The permeation of K^+ remained negligible, while the final concentration of Na^+ ions in the catholyte was around 100 mM for all treated or untreated membranes (Figure 5E). However, some enhanced transport was observed for anions through elongated chlorine-treated membranes: final ClO_4^- concentration in catholyte changed from 1.3 mM (pristine) to 4.3 mM (2 h) and 6.2 mM (24 h) with treatment, and the final Cl^- concentration in the anolyte increased from 11.9 to 17.7 mM (2 h) and 18.5 mM (24 h) (Figure 5E). Nevertheless, the overall impact of the PA layer selectivity on the ion transport in the electro-driven process in the electrolyzer is less apparent compared to its impact in the pressure-driven filtration process. For instance, it has been reported that the salt rejection capability of the PA membrane for reverse osmosis process was nearly eliminated with chlorine treatment with a reduction of NaCl rejection from 97% to less than 20%.[33] This observed ion permeation also corroborates our conclusion that the PA layer selectivity of the composite membranes plays a much less significant role in determining the applied voltage of the seawater electrolyzer.

Clarifying Mechanisms of Ion Transport through Modeling. The diffusion-electromigration model of ion transport during the electrolysis was used to understand the small impact of the PA layer pore size on the separation selectivity in the electro-driven process. The dependence of the membrane resistance on the pore size within the PA layer was first calculated to estimate the pore size change due to chlorine treatment (Figure 6A). Results indicate that when assuming a typical pore diameter for a pristine TFC membrane of 0.5 nm,[17] a decrease in the membrane resistance by 50% (in 10 mM $NaClO_4$) would require a double average pore size (~1.0 nm). This rapid resistance decline highlights the significance of steric confinement in impacting the ion permeation through the PA layer. Further enlargement of the PA layer pores from 1.0 to 10.0 nm leads to an additional 14% decrease in the membrane resistance, with the remaining membrane resistance likely contributed by the support layer of the composite membrane.

The calculated dependence of the ionic resistance on the PA pore size is also consistent with our measurement with chlorine-treated membranes. With only 2 h of treatment using NaClO, the ionic resistance of the composite membranes ($NaClO_4$ tests) decreased to 54%, while with 24 h chlorination the resistance decreased to 33% of its original value. Model simulations indicated that pores larger than 2.5 nm represent the PA membranes with 24 h chlorine treatment (67% decline) (Figure 6A), as this is in a region where pore size is predicted to have a low impact on ion permeation. In the electrolyzer simulations we therefore used pore sizes of 0.5 nm for the pristine membranes and 2.5 nm for the chlorine-treated ones.

https://doi.org/10.1021/acs.est.3c04768
Environ. Sci. Technol. 2023, 57, 14569−14578

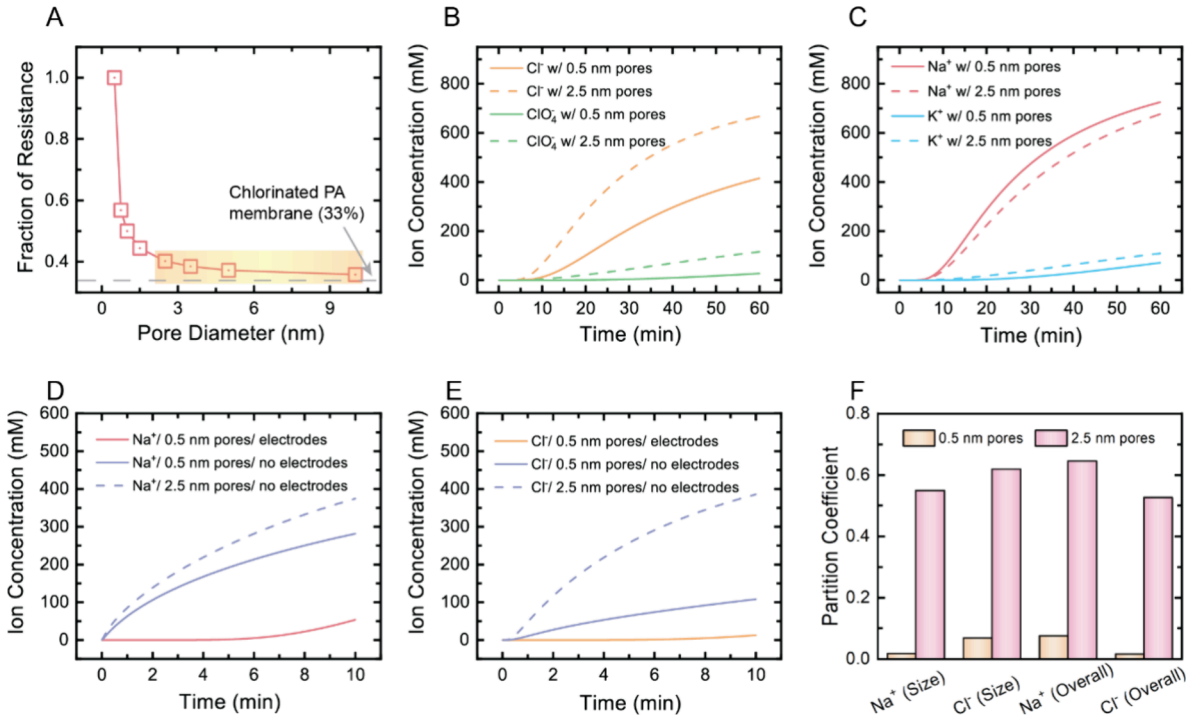

Figure 6. Calculations of ion transport through PA membranes within the electrolyzer. (A) Dependence of the membrane resistance on the membrane pore size. (B) Cl^- and ClO_4^- permeation through the PA membrane (pristine: solid line; enlarged pores: dashed line) within the electrolyzer. (C) Na^+ and K^+ permeation through pristine and pore-enlarged PA membrane within the electrolyzer. (D) Na^+ transport through the pristine PA membrane within the electrolyzer with/without the electrode resistance (solid lines) and through the enlarged-pore membrane without the electrode resistance. (E) Cl^- transport through the pristine PA membrane in the electrolyzer with/without the electrode resistance and through the pore-enlarged membrane without the electrode resistance. (F) Size-dependent partition coefficients and overall partition coefficients for Na^+ and Cl^- ions with the pristine PA membrane and the PA membrane with enlarged pores.

This approach neglects changes in porosity that can also impact the rate of ion crossover. Therefore, by using a constant porosity, we likely overestimated the actual pore diameter after chlorination. For our purpose here, however, using only a change in pore size was sufficient to examine the impact of membrane selectivity toward ion permeation during electrolysis.

Model results indicated that the transport of Na^+ through the pristine PA membrane was the greatest among all of the hydrated salt ions, followed by Cl^- ions (Figure S7A), consistent with our experimental measurements. The catholyte pH underwent a significant increase initially and eventually stabilized at 13.5 (Figure S7B). Compared with ion transport through the pristine PA membrane, considerable enhancement in the permeation of Cl^- and ClO_4^- was predicted through the PA membrane with 2.5 nm pores (Figure 6B). Although the simulated concentration values deviate from the experimental observations, the calculated extent of Cl^- transport enhancement when changing the pore size from 0.5 to 2.5 nm is the same as our experimental measurement (1.6 times). There were much smaller changes predicted for cation transport (Figure 6C), e.g., only a 6% change in Na^+ permeation with the increased pore size. The model results here should be interpreted mostly in a qualitative way (reflecting trends rather than accurate values) due to simplifications made in this preliminary model (e.g., the electrolyte recycling through external reservoirs was neglected).

One possible reason for the limited dependence of the cation (e.g., Na^+) passage on the PA pore size is that other components of the electrolyzer system, such as the carbon electrodes, dominated the resistance to cation transport. To test this hypothesis, the diffusivity of salt ions within the carbon electrodes was changed from their bulk water diffusivity (Table S1) to very large values to minimize the electrode resistance to ion transport. With this reduced electrode resistance, the concentration of Na^+ in the catholyte after 10 min of operation was predicted to increase from 50 to 280 mM (Figure 6D), supporting the crucial role of carbon electrodes in the overall resistance to Na^+ transport within the electrolyzer. With the enlarged pore size, the Na^+ concentration in the catholyte increased again by 1.3 times. As a comparison, the concentration of Cl^- ions within the anolyte was predicted to increase by 3.6 times (Figure 6E).

To further explore the mechanisms underlying the limited impact of the PA pore size on the Na^+ transport compared to Cl^- ions, both the size-dependent partition coefficient (only considering size exclusion and dielectric exclusion, $\Phi_{st,i}\Phi_{B,i}$) and the overall partition coefficient ($\Phi_{st,i}\Phi_{D,i}\Phi_{B,i}$) were calculated for Na^+ and Cl^- ions (Figure 6F). When the pore size increased from 0.5 to 2.5 nm, the size-dependent partition factor increased 31 times for Na^+ (from 0.018 to 0.55) and only 9.1 times for Cl^- (from 0.068 to 0.62). The significantly lower size-dependent partition for Na^+ within the small pores mainly results from the larger Stokes radius (0.18 nm for Na^+, 0.12 nm for Cl^-; Table S1). When Donnan effects are also included, the overall partitioning coefficient is 0.074 for Na^+ and 0.016 for Cl^-; thus, Cl^- is rejected 4.6 times more than Na^+. This highlights the fact that a negative membrane charge slows down the permeation of co-ions (Cl^-), according to the charge neutrality principle. Therefore, when the PA layer pore

https://doi.org/10.1021/acs.est.3c04768
Environ. Sci. Technol. 2023, 57, 14569−14578

size was enlarged from 0.5 to 2.5 nm, the overall partition coefficient of Na^+ is increased by 8.6 times (from 0.075 to 0.646), while that of Cl^- ions increased by 33 times (from 0.016 to 0.528), leading to the observed more significant change in Cl^- transport compared to Na^+ ions.

Implications. Based on these results, there are several paths for optimizing TFC membranes for applications in seawater electrolysis. The combination of Donnan partitioning and steric hindrance successfully contained negatively charged Cl^- ions in the cathodic compartment during electrolysis. Adjusting the polyamide pore size did not significantly change the total voltage requirement for electrolysis in comparison to changes in the thickness of the PET support layer. This suggests that polyamide layers should be synthesized denser and more highly charged without appreciably increasing overpotentials and therefore energy use for water electrolysis. Synthesizing membranes with thinner supporting layers and dense, size-selective, and highly negatively charged active layers could further hinder Cl^- transport to the anode and simultaneously reduce the applied potential required for electrolysis. Additional investigations into reducing the Nernst overpotential with either buffered electrolytes or avoiding recirculation of the catholyte could lead to more energy-efficient and cost-effective saltwater electrolysis for green hydrogen gas production.

■ ASSOCIATED CONTENT

Supporting Information

The Supporting Information is available free of charge at https://pubs.acs.org/doi/10.1021/acs.est.3c04768.

> Electrode preparation; parameters used in the numerical model; four-electrode system for the resistance measurement; zero-gap flow for seawater electrolysis; pH of electrolytes at the end of operation; EIS spectra of the electrolyzer system; ion permeation through TFC membranes with a modified support layer; ion permeation through TFC membranes with a modified active layer; and calculated ion permeation through the pristine TFC membrane (PDF)

■ AUTHOR INFORMATION

Corresponding Author

Bruce E. Logan − *Department of Civil and Environmental Engineering, The Pennsylvania State University, University Park, Pennsylvania 16802, United States; Department of Chemical Engineering, The Pennsylvania State University, University Park, Pennsylvania 16802, United States;* orcid.org/0000-0001-7478-8070; Phone: +1 (814) 8637908; Email: blogan@psu.edu

Authors

Xuechen Zhou − *Department of Civil and Environmental Engineering, The Pennsylvania State University, University Park, Pennsylvania 16802, United States;* orcid.org/0000-0001-8007-4787

Le Shi − *Department of Civil and Environmental Engineering, The Pennsylvania State University, University Park, Pennsylvania 16802, United States; College of Environmental and Resource Sciences, Zhejiang University, Hangzhou 310058, P. R. China;* orcid.org/0000-0003-1794-1256

Rachel F. Taylor − *Department of Chemical Engineering, The Pennsylvania State University, University Park, Pennsylvania 16802, United States;* orcid.org/0000-0002-2576-8193

Chenghan Xie − *Department of Civil and Environmental Engineering, The Pennsylvania State University, University Park, Pennsylvania 16802, United States;* orcid.org/0000-0002-4962-9737

Bin Bian − *Department of Civil and Environmental Engineering, The Pennsylvania State University, University Park, Pennsylvania 16802, United States;* orcid.org/0000-0001-5270-4964

Cristian Picioreanu − *Water Desalination and Reuse Center (WDRC), Biological and Environmental Science and Engineering Division (BESE), King Abdullah University of Science and Technology (KAUST), Thuwal 23955, Saudi Arabia*

Complete contact information is available at: https://pubs.acs.org/10.1021/acs.est.3c04768

Notes

The authors declare no competing financial interest.

■ ACKNOWLEDGMENTS

This research was funded by National Science Foundation grant CBET-2027552 and Penn State University through the Stan and Flora Kappe endowment

■ REFERENCES

(1) Dubey, P. K.; Sinha, A. S. K.; Talapatra, S.; Koratkar, N.; Ajayan, P. M.; Srivastava, O. N. Hydrogen generation by water electrolysis using carbon nanotube anode. *Int. J. Hydrogen Energy* **2010**, *35* (9), 3945−3950.

(2) Horri, B. A.; Choolaei, M.; Chaudhry, A.; Qaalib, H. A highly efficient hydrogen generation electrolysis system using alkaline zinc hydroxide solution. *Int. J. Hydrogen Energy* **2019**, *44* (1), 72−81.

(3) Chi, J.; Yu, H. M. Water electrolysis based on renewable energy for hydrogen production. *Chinese J. Catal.* **2018**, *39* (3), 390−394.

(4) Gibson, T. L.; Kelly, N. A. Predicting efficiency of solar powered hydrogen generation using photovoltaic-electrolysis devices. *Int. J. Hydrogen Energy* **2010**, *35* (3), 900−911.

(5) Mässgård, H.; Jonsson, A.*An industrial perspective on ultrapure water production for electrolysis: A techno-economic assessment of membrane distillation for electrolysis-synergies, performance, costs, and value propositions*; KTH Royal Institute of Technology, 2021, Dissertation.

(6) Rossi, R.; Hall, D. M.; Shi, L.; Cross, N. R.; Gorski, C. A.; Hickner, M. A.; Logan, B. E. Using a vapor-fed anode and saline catholyte to manage ion transport in a proton exchange membrane electrolyzer. *Energy Environ. Sci.* **2021**, *14* (11), 6041−6049.

(7) Logan, B. E.; Shi, L.; Rossi, R. Enabling the use of seawater for hydrogen gas production in water electrolyzers. *Joule* **2021**, *5* (4), 760−762.

(8) Yu, L.; Zhu, Q.; Song, S. W.; McElhenny, B.; Wang, D. Z.; Wu, C. Z.; Qin, Z. J.; Bao, J. M.; Yu, Y.; Chen, S.; Ren, Z. F. Non-noble metal-nitride based electrocatalysts for high-performance alkaline seawater electrolysis. *Nat. Commun.* **2019**, *10*, 5106.

(9) Shi, L.; Rossi, R.; Son, M.; Hall, D. M.; Hickner, M. A.; Gorski, C. A.; Logan, B. E. Using reverse osmosis membranes to control ion transport during water electrolysis. *Energy Environ. Sci.* **2020**, *13* (9), 3138−3148.

(10) Zhou, X. C.; Zhao, Y. Y.; Kim, S. R.; Elimelech, M.; Hu, S.; Kim, J. H. Controlled TiO_2 growth on reverse osmosis and nanofiltration membranes by atomic layer deposition: mechanisms and potential applications. *Environ. Sci. Technol.* **2018**, *52* (24), 14311−14320.

(11) Zhou, X. C.; Wang, Z. X.; Epsztein, R.; Zhan, C.; Li, W. L.; Fortner, J. D.; Pham, T. A.; Kim, J. H.; Elimelech, M. Intrapore energy barriers govern ion transport and selectivity of desalination membranes. *Sci. Adv.* **2020**, *6* (48), No. eabd9045.
(12) Kimani, E. M.; Pranic, M.; Porada, S.; Kemperman, A. J. B.; Ryzhkov, I. I.; van der Meer, W. G. J.; Biesheuvel, P. M. The influence of feedwater pH on membrane charge ionization and ion rejection by reverse osmosis: An experimental and theoretical study. *J. Membr. Sci.* **2022**, *660*, No. 120800.
(13) Du, N. Y.; Roy, C.; Peach, R.; Turnbull, M.; Thiele, S.; Bock, C. Anion-exchange membrane water electrolyzers. *Chem. Rev.* **2022**, *122* (13), 11830−11895.
(14) Jang, M. J.; Yang, S. H.; Park, M. G.; Jeong, J.; Cha, M. S.; Shin, S. H.; Lee, K. H.; Bai, Z. Y.; Chen, Z. W.; Lee, J. Y.; Choi, S. M. Efficient and durable anion exchange membrane water electrolysis for a commercially available electrolyzer stack using alkaline electrolyte. *ACS Energy Lett.* **2022**, *7* (8), 2576−2583.
(15) Yuzer, B.; Selcuk, H.; Chehade, G.; Demir, M. E.; Dincer, I. Evaluation of hydrogen production via electrolysis with ion exchange membranes. *Energy* **2020**, *190*, No. 116420.
(16) Epsztein, R.; Shaulsky, E.; Qin, M.; Elimelech, M. Activation behavior for ion permeation in ion-exchange membranes: Role of ion dehydration in selective transport. *J. Membr. Sci.* **2019**, *580*, 316−326.
(17) Wang, L.; Cao, T. C.; Dykstra, J. E.; Porada, S.; Biesheuvel, P. M.; Elimelech, M. Salt and water transport in reverse osmosis membranes: beyond the Solution-Diffusion model. *Environ. Sci. Technol.* **2021**, *55* (24), 16665−16675.
(18) Hajiaghaee, S. F.; Bozorg, A.; Norouzi, M. Forward osmosis performance of thin film composite membrane composed of electrospun polysulfone fiber coated by Fe3O4/fCNT-embedded polyamide active layer. *Korean J. Chem. Eng.* **2022**, *39* (9), 2405−2413.
(19) Chen, X.; Verbeke, R.; Boo, C.; Dickmann, M.; Egger, W.; Ndamage, K.; Vankelecom, I. F. J.; Yip, N. Y. Elucidating the roles of polyamide layer structural properties in the permeability-selectivity tradeoff governing aqueous separations. *ACS ES&T Eng.* **2022**, *2* (10), 1857−1870.
(20) Do, V. T.; Tang, C. Y. Y.; Reinhard, M.; Leckie, J. O. Effects of chlorine exposure conditions on physiochemical properties and performance of a polyamide membrane-mechanisms and implications. *Environ. Sci. Technol.* **2012**, *46* (24), 13184−13192.
(21) McCallum, C.; Gabardo, C. M.; O'Brien, C. P.; Edwards, J. P.; Wicks, J.; Xu, Y.; Sargent, E. H.; Sinton, D. Reducing the crossover of carbonate and liquid products during carbon dioxide electroreduction. *Cell Rep. Phys. Sci.* **2021**, *2* (8), No. 100522.
(22) Ritt, C. L.; Werber, J. R.; Wang, M. Y.; Yang, Z. Y.; Zhao, Y. M.; Kulik, H. J.; Elimelech, M. Ionization behavior of nanoporous polyamide membranes. *Proc. Natl. Acad. Sci. U. S. A.* **2020**, *117* (48), 30191−30200.
(23) Deen, W. M. Hindered transport of large molecules in liquid-filled pores. *AIChE J.* **1987**, *33* (9), 1409−1425.
(24) Guzmangarcia, A. G.; Pintauro, P. N.; Verbrugge, M. W.; Hill, R. F. Development of a space-charge transport model for ion-exchange membranes. *AIChE J.* **1990**, *36* (7), 1061−1074.
(25) Born, M. Volumen und hydratationswïrme der ionen. *Zeitschrift ̈fr physik* **1920**, *1* (1), 45−48.
(26) Atkins, P.; Atkins, P. W.; de Paula, J.*Atkins' physical chemistry*; Oxford University Press, 2014, p. 1005.
(27) Urbansky, E. T. Quantitation of perchlorate ion: Practices and advances applied to the analysis of common matrices. *Crit. Rev. Anal. Chem.* **2000**, *30* (4), 311−343.
(28) Epsztein, R.; DuChanois, R. M.; Ritt, C. L.; Noy, A.; Elimelech, M. Towards single-species selectivity of membranes with subnanometre pores. *Nat. Nanotechnol.* **2020**, *15* (6), 426−436.
(29) Calio, P. B.; Li, C. H.; Voth, G. A. Molecular origins of the barriers to proton transport in acidic aqueous solutions. *J. Phys. Chem. B* **2020**, *124* (40), 8868−8876.
(30) Gileadi, E.; Kirowa-Eisner, E. Electrolytic conductivity-the hopping mechanism of the proton and beyond. *Electrochim. Acta* **2006**, *51* (27), 6003−6011.
(31) Louie, J. S.; Pinnau, I.; Reinhard, M. Effects of surface coating process conditions on the water permeation and salt rejection properties of composite polyamide reverse osmosis membranes. *J. Membr. Sci.* **2011**, *367* (1−2), 249−255.
(32) Tong, T. Z.; Zhao, S.; Boo, C.; Hashmi, S. M.; Elimelech, M. Relating silica scaling in reverse osmosis to membrane surface properties. *Environ. Sci. Technol.* **2017**, *51* (8), 4396−4406.
(33) Choi, W.; Choi, J.; Bang, J.; Lee, J. H. Layer-by-Layer assembly of graphene oxide nanosheets on polyamide membranes for durable reverse-osmosis applications. *ACS Appl. Mater. Interfaces* **2013**, *5* (23), 12510−12519.

https://doi.org/10.1021/acs.est.3c04768
Environ. Sci. Technol. 2023, 57, 14569−14578